

# High-Refractive-Index Waveguide Platforms for Chemical and Biosensing

Katrin Schmitt and Christian Hoffmann

**Abstract** The field of chemical and biosensors based on waveguide technology is rapidly growing, with new developments focusing on higher sensitivity and stability. This key demand is prompting researchers and developers to explore new materials for waveguide sensor systems, with especially high-refractive-index materials as promising components. This chapter gives an overview of different sensor platforms implementing high-refractive-index waveguide materials, with applications in both research and commercial sensor systems. This is accompanied by a theoretical background of waveguide-sensing principles, especially focusing on the key steps to high sensor sensitivities.

**Keywords** Evanescent field · Label-free · Fluorescence · Biosensor

## Contents

1	Introduction .....	23
2	Waveguide Theory .....	24
2.1	Ray-Optics Approach .....	25
2.2	Electromagnetic Approach .....	28
3	Waveguide Fabrication Technologies .....	34
4	Light Coupling .....	34
5	Waveguide Materials .....	35
6	Sensor Principles Based on High-Refractive-Index Optical Waveguides .....	36
6.1	Grating-Based Label-Free Detection Systems .....	37
6.2	Interferometric Systems .....	40
6.3	Evanescent Field Fluorescence .....	45

---

K. Schmitt

Fraunhofer Institute for Physical Measurement Techniques, Heidenhofstr. 8, 79110 Freiburg, Germany

C. Hoffmann (✉)

Institute for Bioprocessing and Analytical Measurement Techniques, Rosenhof, 37308 Heilbad Heiligenstadt, Germany

e-mail: christian.hoffmann@iba-heiligenstadt.de

7	Commercial Sensor Systems .....	47
8	Applications .....	49
9	Concluding Remarks .....	51
	References .....	51

## Abbreviations

CCD	Charge coupled device
DNA	Deoxyribonucleic acid
MZI	Mach-Zehnder-Interferometer
RNA	Ribonucleic acid

## Symbols

$c$	Speed of light in vacuum
$d$	Thickness, diameter, distance
$d_{\text{eff}}$	Effective thickness of the waveguide
$\vec{D}$	Electric displacement
$\vec{E}$	Electric field
$\vec{H}$	Magnetic field
$i$	Imaginary unit
$k$	Wave vector
$L$	Interaction length
$m$	Mode number
$n$	Refractive index
$n_a$	Refractive index of the ambient medium
$n_{\text{ad}}$	Refractive index of the surface adlayer
$n_{\text{eff}}$	Effective refractive index of the waveguide
$n_w, n_c, n_s$	Refractive index of waveguide, cover and substrate
$P$	Light intensity
$P_{\text{in}}$	Input power
$P_{\text{out}}$	Output power
$t_{\text{ad}}$	Thickness of the surface adlayer
TE	Transverse electric
TM	Transverse magnetic
$\Delta z$	Penetration depth
$\alpha$	Coupling angle
$\beta_m$	Propagation constant of the mode $m$
$\Delta\Gamma$	Mass coverage
$\varepsilon$	Permittivity

$\overline{\varphi}_{cr}$	Critical angle
$\Delta\phi$	Phase shift
$\kappa$	Diffraction order
$\lambda$	Wavelength
$\lambda_0$	Wavelength in vacuum
$\Lambda$	Grating period
$\mu$	Permeability
$\tau_r$	Phase shift upon reflection
$\omega$	Angular frequency

## 1 Introduction

Nowadays, chemical sensors and biosensors play a crucial part in everyday life. In the wide field of sensors, those based on waveguide-sensing principles are used, for example, for routine analyses, and more generally, for many applications in physics, chemistry, biology, or medical and pharmaceutical tasks [1–3]. The versatility of waveguide-based sensors combined with their high sensitivity has paved the way for such sensor platforms to play a role in the wide range of possible applications – with many more waiting to be explored. Yet, one crucial prerequisite for the success of a technology is sensitivity, and the sensitivity of waveguides is directly linked to their refractive index. Due to this, waveguide materials with a high refractive-index have attracted recent attention towards the development of new sensors. In addition to the refractive index of the waveguide material, the so-called evanescent field can be optimized to reach high sensor sensitivity. The evanescent field is the exponentially decaying part of the guided light wave lying outside the waveguide. Evanescent field sensors, as presented in this chapter, use this effect to measure the interaction between the sample and the evanescent field. Such sensors can operate either in a label-free manner, i.e., they detect the analyte directly without any reporter molecule, or the evanescent field is used to excite fluorophores attached to the analyte, close to the waveguide surface. The advantage of the selective excitation of bound fluorophores within the evanescent field is that the background signal caused by unbound fluorophores is reduced to a large extent.

Here, we focus on different sensor platforms implementing high-refractive-index waveguide materials with applications in research, as well as commercial sensor systems. The chapter starts with a theoretical background of waveguide-sensing principles, describing the important steps to achieve high sensor sensitivities. This is followed by the introduction of common waveguide fabrication technologies, coupling methods, and high-refractive-index waveguide materials. The second part of the chapter is devoted to sensor principles based on high-refractive-index waveguide materials and presents commercially available sensor systems implementing such waveguides.

## 2 Waveguide Theory

The term “waveguide” commonly refers to a structure, i.e., a dielectric medium that is able to confine and guide electromagnetic waves. In the simplest case, the waveguide is a material having a refractive index sufficiently high compared to the ambient medium, and appropriate dimensions, to guide light at distinctive wavelengths by total internal reflections. This principle applies to both planar waveguides and optical fibers, which are known from telecommunications applications. Figure 1 shows the basic setup of planar and fiber optic waveguides. Sensor systems for chemical and biosensing applications implement both types of waveguides, depending on the setup and application.

Based on their dimensions and light-guiding properties, both planar and fiber optical waveguides can be subdivided into two classes, namely, *single-mode* (small waveguide thickness) and *multimode* (comparably large thickness). A light wave reproducing itself after two reflections in the waveguide is called an eigenmode, or simply, mode of a waveguide [4]. In single-mode waveguides, only one light mode can be guided, whereas thicker waveguides allow several modes. For multimode waveguides, a description based on the ray-optics approach is adequate. Yet, it does not suffice to describe thin-film (thin core) waveguides, where the electromagnetic

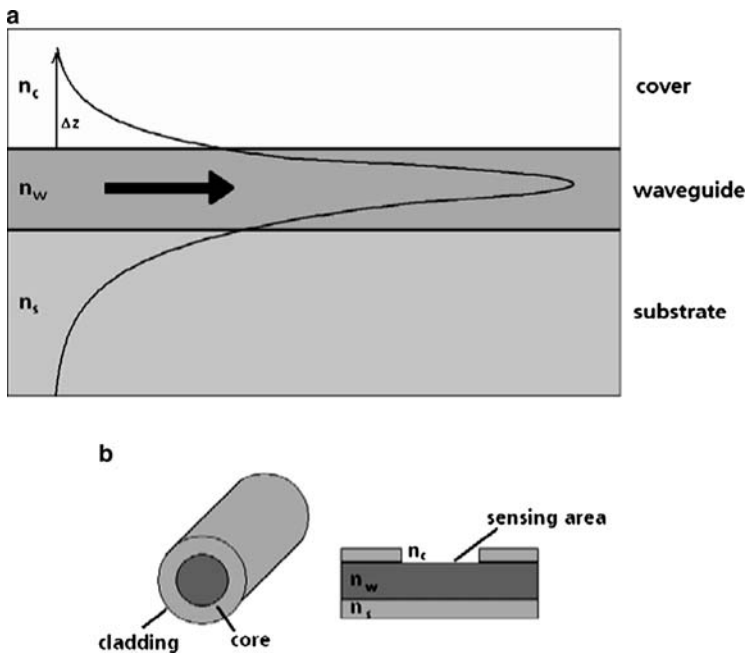


**Fig. 1** (a) Planar waveguide with refractive index  $n_w$  on top of a substrate (refractive index  $n_s$ ). The evanescent field (penetration depth  $\Delta z$ ) of a guided light mode extends into the cover with refractive index  $n_c$ . (b) Optical fiber waveguide. The same conditions apply as to the planar waveguide

approach is more suitable. These two approaches, which are presented in this chapter, basically follow the description of the optical waveguide theory in Snyder and Love [5]. We exclude a description of laterally structured waveguides, which can be found, for example, in the publications by Kogelnik [6].

## 2.1 Ray-Optics Approach

Light propagation in optical waveguides is exactly described by Maxwell's equations. Yet, for multimode waveguides, which obey the condition  $\frac{2\pi d}{\lambda_0} \sqrt{n_w^2 - n_{c/s}^2} \gg 1$  ( $d$  = thickness of the waveguide, diameter for fiber waveguides,  $\lambda_0$  = wavelength of guided light in vacuum,  $n_{w,c/s}$  = refractive index of waveguide, cover, and substrate, respectively; cf. Fig. 1), the classical geometric approach using ray optics provides a good approximation, and can be based either on direct ray tracing along the waveguide, neglecting any wave effects or on a reduction of the solutions of Maxwell's equations to geometric optics. Here, we focus on the ray tracing method and refer to Snyder and Love [5] for further reading. For simplicity, we assume in the following that the waveguide is planar, with no losses due to absorbance or light scattering (*ideal* waveguide) and an unbounded substrate/cover. In an ideal waveguide, light could therefore propagate over arbitrarily large distances with no loss of power. Furthermore, only step-index waveguides with  $n_w = \text{const.}$  are considered, as shown in Fig. 2.

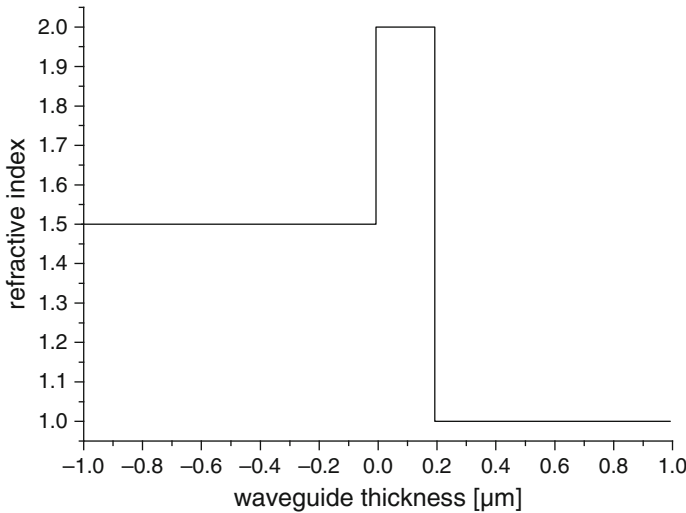


**Fig. 2** Refractive index profile of a 200 nm step-index waveguide with refractive indices of  $n_s = 1.5$ ,  $n_w = 2.0$  and  $n_c = 1.0$

We now consider a light wave with  $\lambda = \lambda_0/n$ , polarized in the  $x$ -direction, traveling in the waveguide between the two interfaces, waveguide-cover and waveguide-substrate. The wave will be reflected at the interfaces with angles  $\varphi_c$  and  $\varphi_s$  for cover and substrate, respectively. Since we assume the electric field is parallel to the interfaces, a phase shift of  $\tau_r$  will occur at each interface according to Fresnel's formulas, while the amplitude and polarization remain the same. Additionally, we assume for simplicity that  $\varphi_c = \varphi_s = \varphi$ .

We now consider only waves that reproduce themselves after two reflections (resonance condition), called *eigenmodes* (or simply *modes*) of the waveguide. These modes have the same transversal field distribution and polarization along the waveguide, which is a direct result of the resonance condition [4]. Figure 3 represents the resonance condition graphically. If we now consider the resonance condition with the help of Fig. 3, i.e., the phase difference needs to be a multiple of  $2\pi$ , we get

$$\frac{2\pi}{\lambda} \overline{AB} = \frac{2\pi}{\lambda} \overline{AC} - 2\pi m - 2\tau_r \quad \text{with } m = 1, 2, 3, \dots \text{ (mode number)} \quad (1)$$

After two reflections, the reflected wave is at a distance of  $\overline{AC} - \overline{AB} = 2d \sin \varphi$  from the original wave:

$$\frac{2\pi}{\lambda} 2d \sin \varphi - 2\tau_r = 2\pi m \quad \text{with } m = 1, 2, 3, \quad (2)$$

The phase shift  $\tau_r$  upon reflection at the interfaces depends on both the angle of reflection  $\varphi$  and on the polarization of the electromagnetic wave (TE or TM).

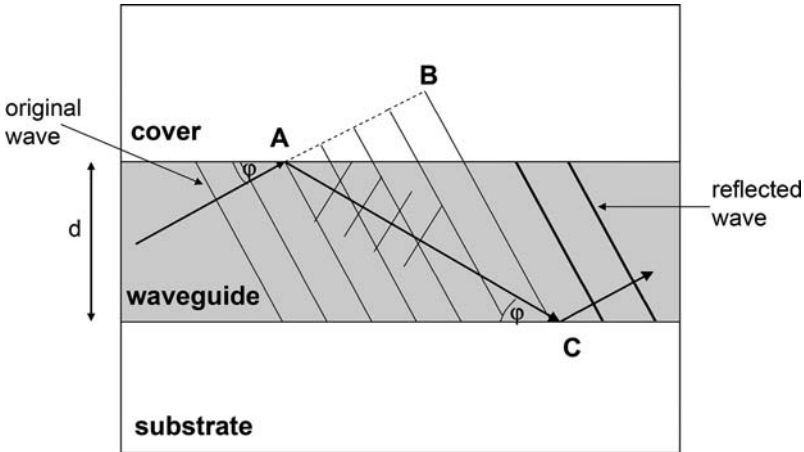


**Fig. 3** Geometrical representation of the resonance condition. The phase difference after two reflections at the boundary layers has to be a multiple of  $2\pi$ . Additionally, a phase shift of  $\tau_r$  occurs at each interface

For TE (electric field is perpendicular to the plane of incidence spanned by the wave normal and the normal to the interface), the phase shift is

$$\tan \frac{\tau_r}{2} = \frac{\sqrt{\sin^2 \bar{\varphi} - \sin^2 \bar{\varphi}_{cr}}}{\cos \bar{\varphi}}, \quad (3)$$

where  $\bar{\varphi}_{cr}$  is the critical angle for total internal reflection and  $\bar{\varphi}$  denotes the angle to the perpendicular. The definition of the *effective refractive index*,

$$n_{\text{eff}} = n_w \sin \bar{\varphi}, \quad (4)$$

which is a measure for the phase velocity of the guided light wave, and together with  $\sin \bar{\varphi}_{cr} = \frac{n_{c/s}}{n_w}$  and  $\cos \bar{\varphi} = \sqrt{n_w^2 - n_{\text{eff}}^2}/n_w$  allows to describe the phase shift in the following form:

$$\tau_r = 2 \arctan \left\{ \frac{n_w \sqrt{\frac{n_{\text{eff}}^2}{n_w^2} - \frac{n_{c/s}^2}{n_w^2}}}{\sqrt{n_w^2 - n_{\text{eff}}^2}} \right\} = 2 \arctan \sqrt{\frac{n_{\text{eff}}^2 - n_{c/s}^2}{n_w^2 - n_{\text{eff}}^2}}. \quad (5)$$

With the wave vector  $k$  and its components,  $k_x = 0$ ,  $k_y = n_w k \sin \bar{\varphi}$  and  $k_z = n_w k \cos \bar{\varphi}$ , we can write this expression, using equation (4), as

$$k d \sqrt{n_w^2 - n_{\text{eff}}^2} - 2 \arctan \sqrt{\frac{n_{\text{eff}}^2 - n_{c/s}^2}{n_w^2 - n_{\text{eff}}^2}} = \pi m. \quad (6)$$

After defining

$$a = k \sqrt{n_w^2 - n_{\text{eff}}^2}, \quad (7)$$

$$b = k \sqrt{n_{\text{eff}}^2 - n_{c/s}^2}, \quad (8)$$

we can rewrite (6) as a transcendental equation for the determination of  $n_{\text{eff}}$ :

$$\tan(ad - \pi m) = \frac{2ab}{a^2 - 2b}. \quad (9)$$

This expression can be solved either graphically or numerically. The solutions are discrete, i.e., the wave can be guided only for certain values of  $n_{\text{eff}}$ , corresponding to one mode. A more detailed description of the graphical solution (mode diagram) follows in the next section.

## 2.2 Electromagnetic Approach

The general description of electromagnetic waves is based on Maxwell's equations. For applications in optics, as that is important here, they reduce to the special case of charge- and current-free media. A subset of the solutions of the Maxwell equations can be assumed to be a harmonic wave of the form:

$$A(t) = A e^{i\omega t}, \quad (10)$$

with the angular frequency  $\omega = 2\pi c/\lambda$ . Inserting this representation and  $\vec{D} = \epsilon \vec{E}$  into Maxwell's equations gives

$$\vec{\nabla} \times \vec{E} = -i\omega\mu\vec{H}, \quad (11)$$

$$\vec{\nabla} \times \vec{H} = i\omega\epsilon\vec{E}, \quad (12)$$

with

$\mu$  = permeability

$\vec{E}$  = electric field

$\vec{H}$  = magnetic field

$\vec{D}$  = electric displacement

$\epsilon$  = permittivity

In the case of a planar waveguide with  $z$  as the direction of light propagation, the solutions to these equations can be described in the following form:

$$A(x, y, z) = A_m(x, y)e^{-i\beta_m z}, \quad (13)$$

with  $\beta_m = \frac{2\pi}{\lambda_0} n_w \sin \varphi$  being the propagation constant and  $m$  the mode index. The mode index is omitted now for simplicity; the different modes of a waveguide are discussed later in greater detail. Inserting (13) in (12) and (11) and separating  $x$ ,  $y$ , and  $z$  yields

$$\frac{\partial E_z}{\partial y} + i\beta E_y = -i\omega\mu H_x, \quad (14)$$

$$i\beta E_x + \frac{\partial E_z}{\partial x} = i\omega\mu H_y, \quad (15)$$

$$\frac{\partial E_y}{\partial x} - \frac{\partial E_x}{\partial y} = -i\omega\mu H_z, \quad (16)$$

$$\frac{\partial H_z}{\partial y} + i\beta H_y = i\omega\epsilon E_x, \quad (17)$$



$$i\beta H_x + \frac{\partial H_z}{\partial x} = -i\omega\epsilon E_y, \quad (18)$$

$$\frac{\partial H_y}{\partial x} - \frac{\partial H_x}{\partial y} = i\omega\epsilon E_z. \quad (19)$$

As stated earlier, the direction of light propagation is  $z$ , and the confinement of the waveguide is in the  $x$ -direction. It is assumed that the waveguide is not structured laterally, i.e., has an infinite extension in the  $y$ -direction. Then, without loss of generality, we can assume that  $\frac{\partial}{\partial y} \equiv 0$ , because under this condition, the electric and magnetic fields supported by the waveguide do not depend on the  $y$ -direction.

From these equations, the mode distribution in waveguides can be calculated. As stated earlier, light waves satisfying the resonance condition, i.e., reproducing themselves after two reflections in the waveguide, are called modes. The mode equation for three-layer planar waveguides has been described by Tiefenthaler and colleagues in the following form [7]:

$$2kd\sqrt{n_w^2 - n_{\text{eff}}^2} + \varphi_c + \varphi_s = 2\pi m. \quad (20)$$

It can be seen directly from the mode equation where  $k = \frac{2\pi}{\lambda_0}$  that with an increasing ratio of thickness  $d$  to the wavelength  $\lambda$ , more modes can be guided. In a planar waveguide, where linearly polarized light is guided, two different modes exist: the TE mode supports only electrical fields perpendicular to the direction of propagation ( $E_z = 0$ ), similarly to the TM mode, where  $H_z = 0$ . Considering this for equations (14)–(19), we get for TE modes:

$$\beta E_y = -\omega\mu H_x, \quad (21)$$

$$\frac{\partial E_y}{\partial x} = -i\omega\mu H_z, \quad (22)$$

$$\frac{\partial H_z}{\partial x} + i\beta H_x = -i\omega\epsilon E_y, \quad (23)$$

and for TM:

$$i\beta E_x + \frac{\partial E_z}{\partial x} = i\omega\mu H_y, \quad (24)$$

$$\beta H_y = \omega\epsilon E_x, \quad (25)$$

$$\frac{\partial H_y}{\partial x} = i\omega\epsilon E_z, \quad (26)$$

where  $\beta$  is the propagation constant. Guided modes, i.e., waves undergoing total internal reflection, are bounded by the following condition:

$$kn_{c/s} \leq \beta \leq kn_w. \quad (27)$$

Inserting this boundary condition into (21)–(26) yields for TE:

$$E_y = Ae^{-\gamma x} \quad \text{for } x \geq 0, \quad (28)$$

$$E_y = A \left( \cos(\delta x) - \frac{\gamma}{\delta} \sin(\delta x) \right) \quad \text{for } 0 \geq x \geq -d, \quad (29)$$

$$E_y = A \left( \cos(\delta h) + \frac{\gamma}{\delta} \sin(\delta h) \right) e^{\alpha(x+h)} \quad \text{for } -d \geq x, \quad (30)$$

and for TM:

$$H_y = Ae^{-\gamma x} \quad \text{for } x \geq 0, \quad (31)$$

$$H_y = A \left( \cos(\delta x) - \left( \frac{n_w}{n_c} \right)^2 \frac{\gamma}{\delta} \sin(\delta x) \right) \quad \text{for } 0 \geq x \geq -d, \quad (32)$$

$$H_y = A \left( \cos(\delta h) + \left( \frac{n_w}{n_c} \right)^2 \frac{\gamma}{\delta} \sin(\delta h) \right) e^{\alpha(x+h)} \quad \text{for } -d \geq x, \quad (33)$$

with  $A$  = arbitrary constant, and

$$\alpha = \sqrt{\beta^2 - k^2 n_s^2}, \quad (34)$$

$$\gamma = \sqrt{\beta^2 - k^2 n_c^2}, \quad (35)$$

$$\delta = \sqrt{k^2 n_w^2 - \beta^2}. \quad (36)$$

To illustrate these results, Fig. 4 shows an example for a normalized field distribution  $H_y$  for a TM mode with index 0.

At the interfaces between the media, the tangential component of  $E_y$  as well as the tangential component of  $H_y$  needs to be continuous. These transition conditions result in a set of linear equations which only yield nontrivial solutions if the coefficient determinant vanishes, and we get the eigenvalue:

$$\tan(\delta d - m\pi) = \frac{\delta(r_c \gamma + r_s \gamma)}{\delta^2 - r_c r_s \gamma \alpha}, \quad (37)$$

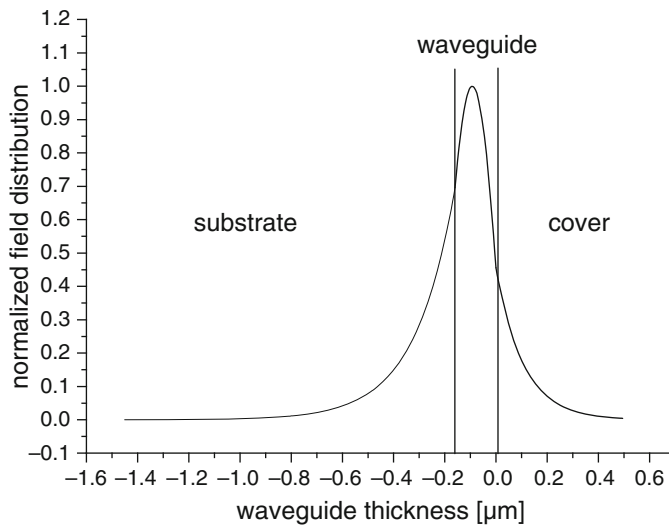


**Fig. 4** TM-mode field distribution for a planar waveguide with refractive indices of  $n_s = 1.52$ ,  $n_w = 2.1$ ,  $n_c = 1.333$  at  $\lambda_0 = 675$  nm, and  $m = 0$  [8]

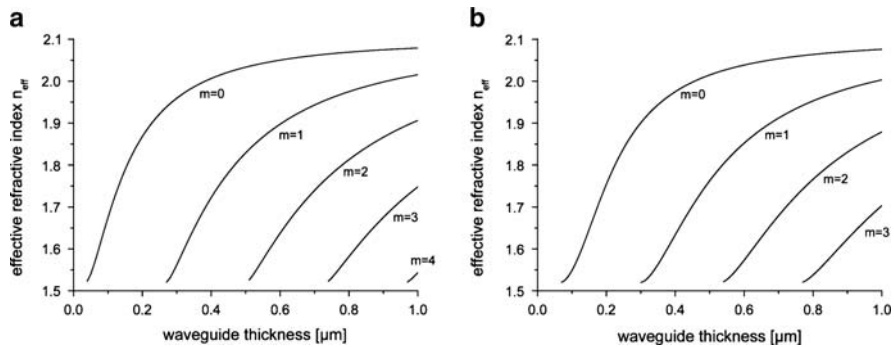


**Fig. 5** Mode diagrams for a dielectric planar waveguide with refractive indices of  $n_s = 1.52$ ,  $n_w = 2.1$ ,  $n_c = 1.333$  at  $\lambda_0 = 675$  nm. (a) TE modes, (b) TM modes [8]

with  $r_{c/s} = 1$  for TE modes and  $r_{c/s} = \left(\frac{n_s}{n_c}\right)^2$  for TM modes. This eigenvalue equation can be solved either graphically or numerically, and has already been found with the ray-optics approach. Figure 5 shows mode diagrams for TE and TM modes using the following parameters:  $n_s = 1.52$ ,  $n_w = 2.1$ ,  $n_c = 1.333$  at  $\lambda_0 = 675$  nm [8].

When the waveguides are used as sensors, i.e., in label-free applications, their sensitivity to changes in the cover layer is important. In the following, again ideal waveguides will be treated, i.e., nonporous ones, so that they react only to changes

on their surface, and diffusion processes into the waveguide layer will be neglected. Two types of surface changes and, thus, the effective refractive index can occur: either, the bulk refractive index changes, e.g., variations in the refractive index of the buffer, or molecules adsorb or bind to the surface, also resulting in a signal change of the effective refractive index. The general expression for changes in  $n_{\text{eff}}$  is given by Tiefenthaler and Lukosz [7]:

$$\Delta n_{\text{eff}} = \left( \frac{\partial n_{\text{eff}}}{\partial t_{\text{ad}}} \right) \Delta t_{\text{ad}} + \left( \frac{\partial n_{\text{eff}}}{\partial n_{\text{c}}} \right) \Delta n_{\text{c}} + \left( \frac{\partial n_{\text{eff}}}{\partial n_{\text{w}}} \right) \Delta n_{\text{w}}, \quad (38)$$

where the last summand can be omitted for nonporous waveguides.  $t_{\text{ad}}$  denotes the thickness of the surface adlayer. It is assumed that the molecules form a homogeneous layer with  $t_{\text{ad}} \ll \lambda_0$ .

From the mode equation and equation (38), the waveguide sensitivity for both cover refractive index and the surface adlayer changes can be derived (three-layer planar waveguide). The derivation is given in detail in [7] and here only the results are given:

$$\frac{\partial n_{\text{eff}}}{\partial n_{\text{c}}} = \left( \frac{n_{\text{c}}}{n_{\text{eff}}} \right) \left( \frac{n_{\text{w}}^2 - n_{\text{eff}}^2}{n_{\text{w}}^2 - n_{\text{c}}^2} \right) \left( \frac{\Delta z_{\text{c/s}}}{d_{\text{eff}}} \right) \left[ 2 \left( \frac{n_{\text{eff}}}{n_{\text{c}}} \right)^2 - 1 \right]^{\rho} \quad (39)$$

for cover refractive index changes, and

$$\frac{\partial n_{\text{eff}}}{\partial t_{\text{ad}}} = \left( \frac{n_{\text{w}}^2 - n_{\text{eff}}^2}{n_{\text{eff}}^2 d_{\text{eff}}} \right) \left( \frac{n_{\text{ad}}^2 - n_{\text{c}}^2}{n_{\text{w}}^2 - n_{\text{c}}^2} \right) \left[ \frac{\left( \frac{n_{\text{eff}}}{n_{\text{c}}} \right)^2 + \left( \frac{n_{\text{eff}}}{n_{\text{ad}}} \right)^2 - 1}{\left( \frac{n_{\text{eff}}}{n_{\text{c}}} \right)^2 + \left( \frac{n_{\text{eff}}}{n_{\text{w}}} \right)^2 - 1} \right]^{\rho} \quad (40)$$

for surface adlayer changes, where  $\Delta z_{\text{c/s}}$  are the penetration depths of the evanescent field into cover (c) and substrate (s), respectively,  $n_{\text{ad}}$  denotes the refractive index of the surface adlayer,  $\rho = 0$  for TE modes and  $\rho = 1$  for TM modes, and

$$d_{\text{eff}} = d + \Delta z_{\text{c}} + \Delta z_{\text{s}} \quad (41)$$

defines the effective thickness of waveguide.

Equations (39) and (40) can again be solved by numerical iteration. Figure 6 shows the sensitivities  $\frac{\partial n_{\text{eff}}}{\partial n_{\text{c}}}$  and  $\frac{\partial n_{\text{eff}}}{\partial t_{\text{ad}}}$  for the first two TE and TM modes (0 and 1). The calculations show higher sensitivities for TM modes, while a waveguide thickness of 150–160 nm yields the optimum sensitivity. The equations also imply that high sensitivities can be reached with monomode waveguides, having a high refractive index difference to the substrate refractive index.

In other cases, when the light in the evanescent field of the waveguides is used to excite fluorophores on the waveguide surface, the light intensity in the evanescent

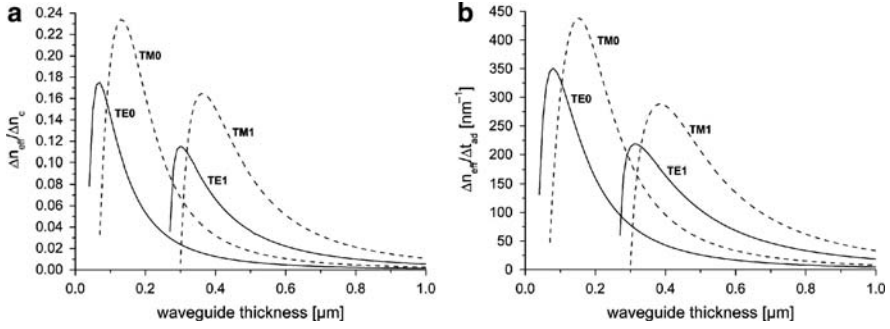


**Fig. 6** Theoretical sensitivities of waveguides depending on the waveguide thickness, (a) to cover refractive index changes, (b) to surface adlayer changes with  $n_s = 1.52$ ,  $n_w = 2.1$ ,  $n_c = 1.333$  at  $\lambda_0 = 675$  nm [8]

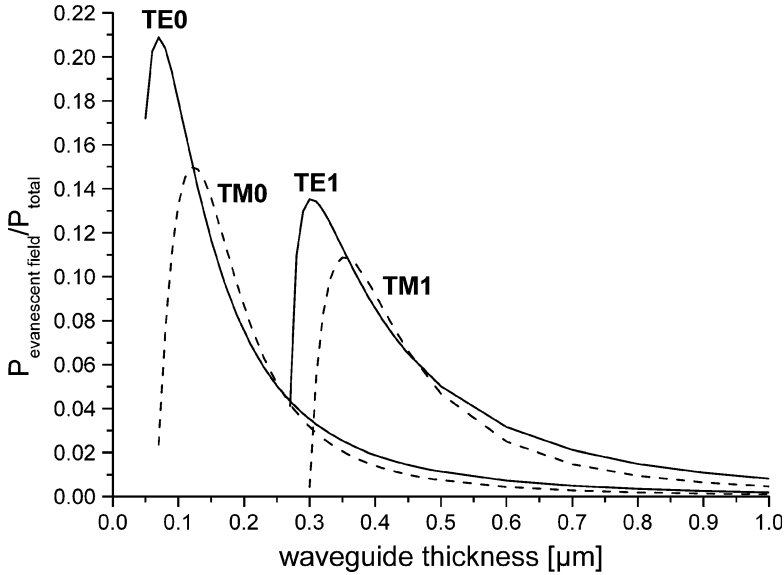


**Fig. 7** Theoretical light intensities in the evanescent field as the fraction of the total light intensity in the waveguide versus waveguide thickness. Parameters for calculation:  $n_s = 1.52$ ,  $n_w = 2.1$ ,  $n_c = 1.333$  at  $\lambda_0 = 675$  nm

field is crucial to optimize the excitation efficiency. Figure 7 depicts the light intensity in the evanescent field as a fraction of the total light intensity in the waveguide, depending on the waveguide thickness, according to the following equation:

$$\frac{P_{\text{evanescent field}}}{P_{\text{total}}} = \left( \frac{n_w^2 - n_{\text{eff}}^2}{n_w^2 - n_c^2} \right) \frac{\Delta z_c}{d_{\text{eff}}}. \quad (42)$$

The TE<sub>0</sub> mode provides the highest light intensity in the evanescent field for monomode waveguides with thicknesses from 60 to 70 nm.

### 3 Waveguide Fabrication Technologies

To achieve high-refractive-index optical waveguides, the appropriate waveguide technology has to be chosen. For chemical and biosensing applications, not only sensitivity is a crucial prerequisite, but also an easy structuring process and the resistance against a wide range of chemicals used for bio-molecule immobilization and their regeneration.

Several technologies have evolved to fabricate optical waveguides, which can be divided into two classes: in the first case, the substrate material is modified, e.g., by ion exchange in SiO<sub>2</sub> or LiNbO<sub>3</sub> [9, 10]. These waveguides have the disadvantage that their refractive index is increased only to a minor extent, yet they show less porosity than coated waveguide layers. In the second case, a waveguide layer is applied on top of a substrate material (coating) as it is done with metal oxides or nitrides [11–14]. Here, high-refractive-index waveguides can be achieved more easily, but often they are porous and lack sufficient chemical resistance. These waveguides are mainly fabricated using chemical vapor deposition techniques (CVD). The need for low porosity in combination with high chemical resistance requires optimized coating techniques to fabricate extremely dense waveguide films, also to reduce surface roughness to minimize light losses due to scattering.

### 4 Light Coupling

Because of the small dimensions of thin-film waveguides, the coupling of light requires special attention. The application of the sensor system and the layout of the waveguide determine the light coupling method. Figure 8 shows four commonly used coupling methods for thin-film waveguides.

Front-face coupling can be accomplished either by a lens focusing a collimated light beam onto the waveguide or by a waveguide illumination with an optical fiber. Effective coupling requires well-prepared (e.g., polished) square edges of the waveguide and an exact alignment of the optical elements focusing the light beam. This ensures a maximal overlap integral, which is determined by the intensity distribution of the light and the distribution of the waveguide modes. Although technically not demanding, front-face coupling has the disadvantage of low robustness against vibrations in the sensor system, and it requires extensive alignment procedures to minimize variations in the coupling efficiency.

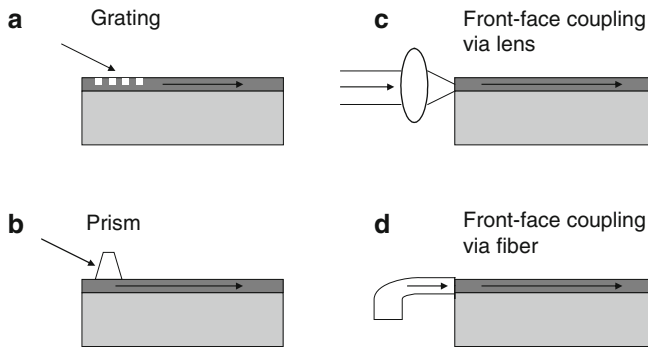


**Fig. 8** Light coupling methods into waveguides. (a) Grating coupling, (b) prism coupling, (c) front-face coupling via optical lens (d) front-face coupling via optical fiber

Prism coupling also requires no waveguide structuring and is a relatively simple method. Light is coupled into the waveguide via an attached prism on the waveguide surface. Compared to front-face coupling, the alignment of the light beam is not as critical as long as the correct coupling angle is used. The coupling angle depends on the effective refractive index of the waveguide.

However, this coupling method might not be suitable for sensor systems used outside the laboratory, since the pressure of the prism on the waveguide needs to be reproduced with high precision.

For grating coupling, a defined grating structure in the waveguide is necessary, which is technically more elaborate than the other methods. As with prism coupling, the coupling angle is determined by the effective refractive index of the waveguide (sensing principle of the grating coupler sensor). The grating structure allows only a very narrow range of coupling angles, depending on the spectral bandwidth of the light source. The position of the light beam on the grating influences the coupling efficiency to a large extent, along with grating parameters, i.e., structure depth. When linearly polarized light is used, the direction of polarization, i.e., TE or TM mode, is decisive. An advantage of this coupling method over the previously mentioned methods is a good reproducibility of coupling conditions since no further optical elements are directly involved.

## 5 Waveguide Materials

Materials that enable light mode propagation are characterized by a high refractive index and a low attenuation  $<3$  dB/cm. Especially, metal oxides or nitrides meet these optical requirements, and hence  $\text{SiO}_2$ ,  $\text{SiO}_x\text{N}_y$ ,  $\text{Si}_3\text{N}_4$ ,  $\text{TiO}_2$ ,  $\text{Ta}_2\text{O}_5$ , and

$\text{Nb}_2\text{O}_5$  are the typical waveguide materials. The first waveguides used for sensor applications were based on silicon oxide–titanium oxide ( $\text{SiO}_2\text{--TiO}_2$ ) ( $n_{632.8} = 1.750\text{--}2.0$  depending on the titanium content, normally  $n_{632.8} = 1.8$  [15]). These can be manufactured by a sol-gel process, but also magnetron-sputtering was applied [16]. The refractive index of pure titanium oxide  $\text{TiO}_2$  is  $n \approx 2.7$ .

Based on thin-film technology, integrated optical waveguiding chips can be produced with silicon oxynitride  $\text{SiO}_x\text{N}_y$ . Depending on the oxygen and nitrogen content, the refractive index can be varied between pure silicon oxide  $\text{SiO}_2$  ( $n_{632.8} = 1.46$ ) and pure silicon nitride  $\text{Si}_3\text{N}_4$  ( $n_{632.8} = 2.01$ ). The specific value can be controlled by the gas flow ratio of oxygen/nitrogen, when depositing these waveguide layers by low-pressure chemical vapor deposition (LPCVD) or plasma-enhanced chemical vapor deposition (PECVD) technologies [17].

Even higher refractive indices for waveguide materials are given for tantalum pentoxide  $\text{Ta}_2\text{O}_5$  ( $n_{632.8} = 2.22$  [18] or between  $n = 2.1$  and  $n = 2.2$  for the red spectral range [19, 20]). These films are commonly deposited by a reactive sputtering process. Niobium oxide  $\text{Nb}_2\text{O}_5$  ( $n = 2.36$ ) is also used as planar-waveguide material [21, 22].

The refractive indices cited for the waveguide materials are approximate values and are usually determined for the He–Ne laser wavelength 632.8 nm or for the red spectral range. Depending on the purity and the porosity of the waveguide material, the refractive index may vary.

## 6 Sensor Principles Based on High-Refractive-Index Optical Waveguides

High-refractive-index materials enable the investigation of bioreactions at the surface within the evanescent field. Various sensor systems were developed with the advantage of high sensitivity and measurement in the presence of the sample without any rinsing. The sensor principles can be divided into label-free sensor systems where the determination of the effective refractive index is the pivotal parameter and systems based on surface-confined fluorescence excitation where the marker molecule is solely detected.

Systems based on the monitoring of refractive-index changes are suitable for the determination of affinity constants and kinetic studies. Grating coupler and interferometric devices were developed for this purpose. The advantage of simple sample preparation without reporter molecule faces the disadvantage of interfering signals caused by nonspecific binding effects of matrix molecules, since the signal depends mainly on the mass coverage on the surface without any discrimination of molecules. Evanescent field fluorescence systems are characterized by the independence of the molecular mass of the target molecule since they only detect the fluorescent label disregarding the properties of the molecule of interest.



## 6.1 Grating-Based Label-Free Detection Systems

### 6.1.1 Grating Coupler

Various gratings with different design have been developed for the energy transfer of a light beam into or out of an optical waveguide. They are characterized by their geometrical dimensions and the grating period (Fig. 9). The different shapes encompass triangular, rectangular, and trapezoidal profiles, but asymmetric profiles are also possible [23]. The measurement principle of the grating coupler for chemical sensing was first discovered and published by Lukosz and Tiefenthaler [24]. They investigated the coupling of a He–Ne laser beam ( $\lambda = 632.8$  nm) into an embossed surface relief grating on a planar waveguide consisting of SiO<sub>2</sub> and TiO<sub>2</sub>. They observed a propagation of the wave within the waveguide if the coupling condition (43) is fulfilled. Yet, this condition changes in the presence of different ambient gases or humidity, and this effect is reversible. It can, thus, also be exploited in such a way that the ambient conditions are adapted to the coupling condition. This phenomenon is explained by an increasing effective thickness of the waveguide or rather the effective refractive index by water and/or gas adsorption. The coupling always occurs at a certain angle of the incident light beam depending on the effective refractive index of the waveguide. In the identical manner, the coupling condition is valid for outcoupling:

$$n_a \sin \alpha = \kappa \frac{\lambda_0}{\Lambda} - n_{\text{eff}}, \quad (43)$$

with  $n_a$  being the refractive index of the ambient medium (air, buffer),  $\alpha$  the coupling angle,  $\kappa$  the diffraction order,  $\lambda_0$  the wavelength in vacuum, and  $\Lambda$  the grating period.

Therefore, various detection principles are applicable to measure the adsorption of a thin layer on a waveguide grating (Fig. 10). This layer may consist of a gas

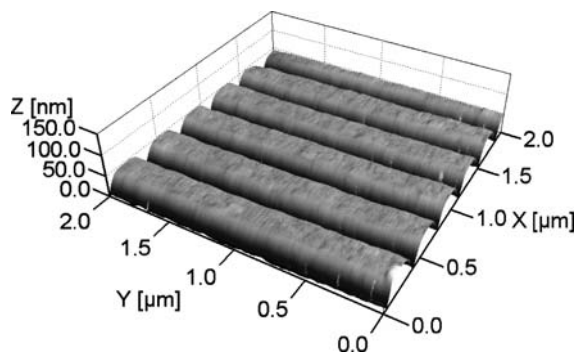


**Fig. 9** Image of a grating area of  $2 \mu\text{m} \times 2 \mu\text{m}$  recorded by atomic force microscopy. Grating depth  $\sim 30$  nm, period  $\sim 330$  nm

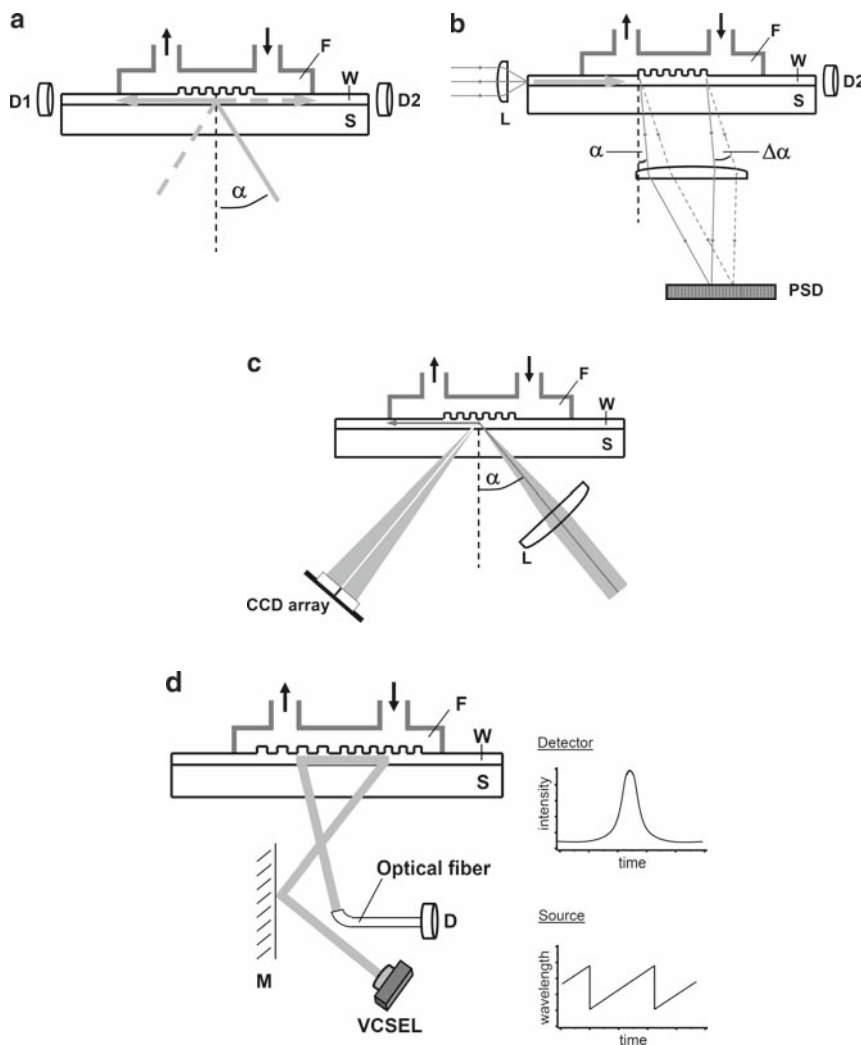


**Fig. 10** Schematic drawings of the various principles of grating coupler systems. (a) input grating coupler [25], (b) output grating coupler [28], (c) reflected-mode grating coupler [30], (d) wavelength-interrogated optical sensor WIOS [19]; *S* substrate, *W* waveguide, *F* fluidic chamber, *L* lens, *PSD* position sensitive detector, *CCD* charge coupled device, *D* photodiode,  $\alpha$  coupling angle,  $\Delta\alpha$  change in coupling angle, *M* mirror (movable), *VCSEL* vertical cavity surface-emitting laser diode

(at different humidity) or any kind of organic matter including biological molecules. The monitoring of the coupling angle of a laser beam into a waveguide via a grating is called *input grating coupler* [25, 26]. A photodetector at the end of the planar waveguide detects the coupling efficiency. The sample can be rotated on

a goniometer to find the coupling angle. The optical arrangement consists only of a coherent light source, collimating lenses, and a photodetector, e.g., a silicon photodiode. The reverse principle, i.e., the detection of the angle of the light beam that propagates first within a waveguide and is then coupled out via a grating, is utilized by the *output grating coupler* [27, 28]. Here, light is coupled into the horizontally positioned waveguide and a position-sensitive photodetector, e.g., a CCD line sensor, monitors the coupling angle depending on the layer thickness or the effective refractive index, respectively. The detected signal then represents the position of the outcoupled light beam on the detector. This arrangement avoids moving parts, leading to a higher signal stability, and therefore higher sensitivity. Another alternative is the *reflection mode grating coupler* that applies an angle spectrum of the light beam to the grating [18, 29, 30]. A collimating lens provides a continuum of angles undergoing reflection except the angle that is obeying the coupling condition. This leads to a dark line corresponding to the coupling angle at the effective refractive index in the reflected light, which is detected by an array detector, e.g., a CCD camera. The latter method suits best for a parallel readout of signals and is, therefore, most promising for high throughput applications and commercialization of such sensor systems since there are no moving parts necessary for the optical readout.

While the aforementioned methods are based on the detection of the coupling angle at a constant wavelength, it is also feasible to keep the incident angle constant and scan the wavelength with a system which is called the *wavelength interrogated optical sensor* (WIOS) [19]. A vertical cavity surface-emitting laser diode (VCSEL) with a saw-tooth wavelength modulation of 2 nm serves as a light source that is directed towards the grating by an adjustable mirror. The coupling condition is fulfilled at a certain wavelength combined with a fixed angle. The light mode is guided through the waveguide and is coupled out by a second grating. Then, the light beam is collected by an optical fiber and detected by a photodiode. The resonance wavelength changes with refractive index variations of the adjacent medium on the surface of the waveguide.

### 6.1.2 Colorimetric Resonant Grating Reflection

Another approach that is also suitable for a parallel readout of binding events is *colorimetric resonant reflection* at a grating with subwavelength structures (Fig. 11) [31, 32]. This is manufactured from a high-refractive-index material and sandwiched between a substrate with lower refractive index, e.g., silicon oxide (glass) and a cover layer that fills the grating grooves, with a lower refractive index as well. The grating exhibits a very small period so that only a sharp wavelength maximum is reflected upon illumination with white light. Consequently, the optical setup consists only of a white light source that illuminates a small spot of the substrate with the grating structure via an optical fiber at normal incidence and a spectrometer that detects the peak wavelength collected by a second fiber, also at normal incidence. When molecules bind to the grating surface, the reflected light shifts

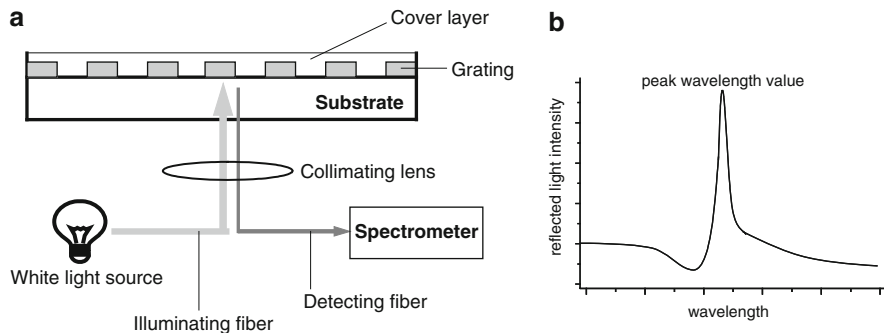


**Fig. 11** (a) Schematic drawing of the colorimetric resonant reflection sensor. White light illuminates the sensor surface by an optical fiber. A second fiber guides the reflected light to a spectrometer. (b) Schematic spectrum

its wavelength due to the change of the optical path of light that is coupled into the grating. Hence, biological molecules like peptides, proteins, or DNA can be detected if the complementary capture molecule is immobilized. Since no coupling optics such as prisms is necessary, the gratings can be implemented in a planar substrate like microtiter plates. This makes it a promising potential high throughput detection system, which is now commercialized by Corning Inc. [21] or SRU Biosystems [33].

## 6.2 Interferometric Systems

Interferometric methods are based on the superposition of two coherent light beams, where one beam has interacted with the sample and the other serves as reference. The superposition of both beams leads to constructive or destructive interferences. Depending on the modulation of the light source, these interferences can be detected simply by a photodiode or laterally resolved by a CCD detector. A variation of the refractive index within the evanescent field, e.g., owing to adsorption of the sample to the waveguide surface, results in a change of the effective refractive index of the waveguide and hence in a phase shift  $\Delta\varphi$ , which can be described as follows:

$$\Delta\varphi = \frac{2\pi}{\lambda_0} L \Delta n_{\text{eff}}, \quad (44)$$

where  $\lambda_0$  denotes the vacuum wavelength and  $L$  the interaction length, i.e., the distance the evanescent field is in contact with the sample. Depending on the experimental approach, the reference branch can compensate intrinsic instabilities due to light source or ambient temperature fluctuations. The most investigated

approach is the so-called *Mach-Zehnder-Interferometer* (MZI) configuration [17, 34]. It consists of one light beam that is split into a sensing and a reference branch. While the sensing branch interacts with the sample, the reference branch is in contact with the reference medium, e.g., air, buffer, solvent, etc., and eventually both branches are combined to interfere. Applying this MZI configuration to a sensor chip means that this structure has to be deposited with a high-refractive-index material on a substrate. When monochromatic light is guided through this waveguide structure, the ratio of the beam power is exactly one and the phase difference is exactly zero if the sensor chip is perfectly manufactured. Applying a sample to the sensing branch, the local refractive index will change at the waveguide surface inducing a phase shift, and the output power will change obeying the following equation:

$$P_{\text{out}} = \frac{1}{2}P_{\text{in}}(1 + \cos \Delta\varphi). \quad (45)$$

Here,  $P_{\text{out}}$  denotes the output power,  $P_{\text{in}}$  the input power, and  $\Delta\varphi$  the sample-induced phase shift. The MZI is generally designed as a system using a monomode wave propagating through the waveguide. The phase shift as a measure for the sample concentration can be derived from the power ratio  $P_{\text{out}}/P_{\text{in}}$ . This implies that in addition to  $P_{\text{out}}$ ,  $P_{\text{in}}$  also has to be determined by a second photodetector. Since the power ratio is a sinusoidal function of  $\Delta\varphi$ , there are the following ambiguities (Fig. 12) inherent in the MZI:

- The fringe order ambiguity: the periodical function leads to equally probable solutions of  $\Delta\varphi$  for a measured value of  $P_{\text{out}}/P_{\text{in}}$ :  $\Delta\varphi' = \Delta\varphi + k2\pi$ , with  $k$  being an integer.
- The directional ambiguity: starting on the sinusoidal function from one extremum, the sign of the slope for a  $\Delta\varphi$  value cannot be deduced leading to different  $\Delta\varphi$  values for one  $P_{\text{out}}/P_{\text{in}}$  value depending on the location on the right- or left-hand side of the extremum.

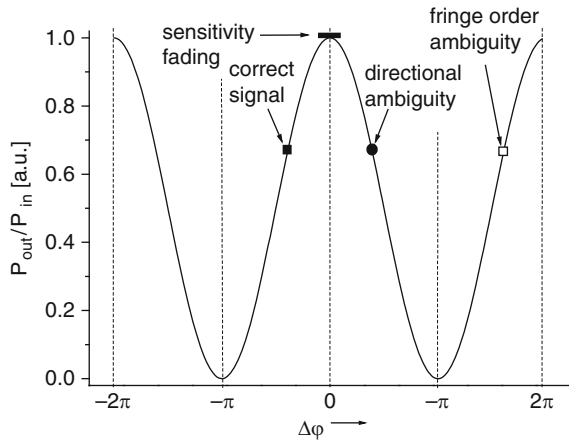


**Fig. 12** Output/input power ratio  $P_{\text{out}}/P_{\text{in}}$  as a function of the phase difference  $\Delta\varphi$  between the sensing and the reference branch illustrating the inherent problems of determining  $\Delta\varphi_m$

- Sensitivity fading: since the slope at the extrema is zero, for  $P_{\text{out}}/P_{\text{in}}$  values equal to zero or one,  $\Delta\varphi$  values are not determinable with high sensitivity. The highest sensitivity can be obtained at the points with the steepest slope at  $\Delta\varphi = (n + \frac{1}{2})\pi$  with  $n$  being an integer.

The problems of directional ambiguity and sensitivity fading can be overcome by a phase modulation of the light source. If the branches are not identical or the splitting or combining of the beam is imperfect, then the MZI system has to be calibrated and an offset value measuring the blank determined:  $\Delta\varphi_{\text{m}} = \Delta\varphi + \Delta\varphi_0$  with  $\Delta\varphi_{\text{m}}$  as measured value and  $\Delta\varphi_0$  as offset value.

With a photodetector allowing lateral resolution, e.g., a CCD camera, an interferometric approach based on the Young double-slit experiment (Thomas Young, 1773–1829) can be carried out. In the *Young-Interferometer* system, the sensing beam and the reference beam being identical abandon the sensor chip into the free space [11, 20, 35–37]. Sample and reference media are applied to the corresponding branches. Another approach buries the reference waveguide which excludes contact to a reference medium [38, 39]. In both approaches, the beams are diffracted at a double slit in the near-field or the diameter dimension of the diverging exit beams is so small that the exit plane acts as a double slit and they can interfere in the far-field. A CCD detector records the interference pattern.

The spatial power distribution  $P(x)$  is given by

$$P(x) = \frac{1}{2}A(x) \left[ 1 + \cos\left(\frac{2\pi x}{p} + \Delta\varphi + \Delta\varphi_0\right) \right], \quad (46)$$

where  $x$  is the lateral coordinate of the interference pattern,  $A(x)$  the envelope function deriving from the aperture of the waveguide,  $p$  the period of the interferogram,  $\Delta\varphi$  the phase shift, and  $\Delta\varphi_0$  an offset value of the phase shift (Fig. 13).

The period  $p$  is determined by the distance  $D$  from the double slit to the detector and the distance  $d$  between the two slits:

$$p = \frac{\lambda D}{d}. \quad (47)$$

For  $D \gg d$ , the envelope function is determined by the diffraction at the single slits. The width of the interferogram  $B$  is defined by the distance of the two first order minima on each side of the maximum as

$$B = \frac{2\lambda D}{b} \quad (48)$$

with  $b$  denoting the slit width. For an exact recording of the interference pattern, a conventional CCD array with a pixel width considerably smaller than its period can be used. The close distance between the double slit leads to fringes of a period that can be detected without any magnifying lenses. The interferogram can be exploited

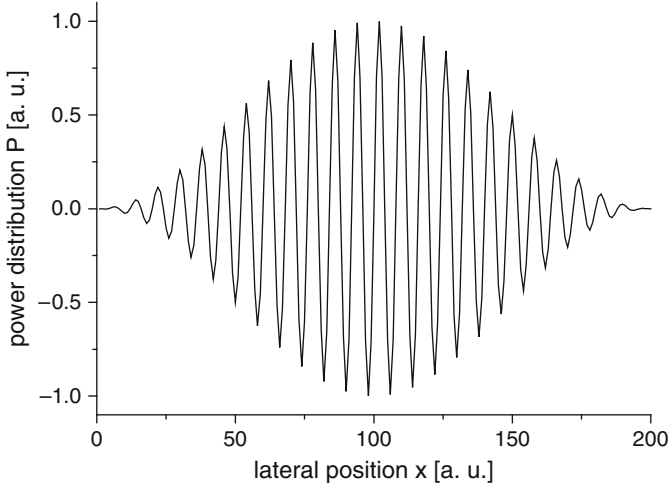


**Fig. 13** Power distribution  $P$  as a function of the lateral coordinate. A phase shift in the wave representing the sensing branch causes a lateral shift of the interference pattern on the CCD detector

by a Fast Fourier Transformation process to obtain the phase shift induced by the sample on the sensing branch and the change of the effective refractive index. The lateral shift  $\Delta x$  of the pattern corresponds to the phase shift  $\Delta\varphi$  by

$$\Delta\varphi = \frac{2\pi}{\lambda} \frac{d}{D} \Delta x. \quad (49)$$

A typical value of the refractive index is assumed so that the layer thickness or mass coverage on the waveguide can be calculated. If the polarization of the light source can be switched between TE and TM, then the refractive index and layer thickness or mass coverage can be determined unambiguously. For each of the two polarization states, the effective refractive index can satisfy a continuous range of thickness and refractive index values. But there is only one combination of values that satisfies the effective refractive index of both the TE and TM modes, simultaneously [38]. The mass coverage  $\Delta\Gamma$  and the refractive index change  $\Delta n_{\text{ad}}$  can be separated as well by using dual wavelength propagating simultaneously through the waveguide or two different waveguide thicknesses [40]

$$\Delta\varphi = \frac{\partial\varphi}{\partial\Gamma} \Delta\Gamma + \frac{\partial\varphi}{\partial n_{\text{ad}}} \Delta n_{\text{ad}}. \quad (50)$$

Since the incremental changes of the mass coverage and the refractive index are different depending on the wavelength and the waveguide thickness, there are two equations to determine the unknown quantities  $\Delta\Gamma$  and  $\Delta n_{\text{ad}}$ .

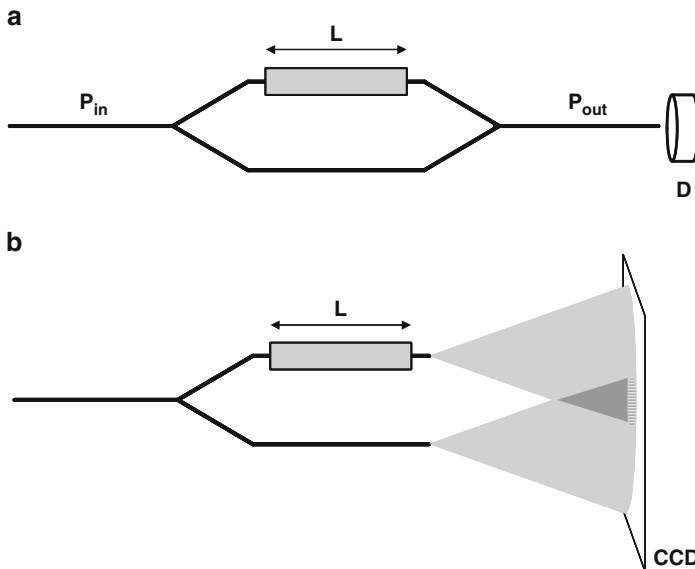


**Fig. 14** Schematic drawings of interferometric arrangements: **(a)** Mach-Zehnder configuration: the sensing and the reference branch are combined after the interaction of the sample and a photodiode (D) that records the light intensity time-resolved. **(b)** Young interferometer. The sensing and the reference branch interfere in the far field. The interference pattern is recorded by a CCD. Either the end face of the waveguide structure approximates two point light sources or a double slit can be set in the beam path to generate the interference pattern.  $L$  interaction length,  $P_{in}$  input power,  $P_{out}$  output power

The Young interferometer overcomes the problem of sensitivity fading in the extremum areas since it resolves the signal laterally using a CCD sensor, while the photodetector of a MZI counts the fringes in a time-resolved manner (Fig. 14). But the Young interferometer approach has the same problem of ambiguity as the MZI, unless a semicoherent (or incoherent) light source is used. In this case, the interference pattern is superimposed on the envelope function known from a single slit. With an algorithm resolving the peak of the interference pattern only, the absolute phase value can be determined.

Compared to grating coupler sensors, interferometric systems are more sensitive and exhibit a very high resolution due to the long interaction length (typically in the range of 1–2 cm) of the guided mode with the sample and the high accuracy the phase shift can be measured (Tables 1 and 2). However, this high resolution cannot be exploited in practical biosensing applications since the sensor responds simultaneously to ambient or sample temperature fluctuations or refractive index changes of the sample solution. The contributions of the biosensing, refractometric, and temperature effects to the phase shift are superimposed and cannot easily be distinguished.



**Table 1** Different detection limits of grating coupler sensors

Type	Waveguide material	Citation	Detection limit ( $\Delta n_{\text{eff, min}}$ )	Detection limit by model system
Input	SiO <sub>2</sub> -TiO <sub>2</sub>	[26]	$5 \times 10^{-6}$	6 $\mu\text{g/mL}$ anti-h-IgG to adsorbed h-IgG
	SiO <sub>2</sub> -TiO <sub>2</sub>	[25]	$2 \times 10^{-6}$	0.16 $\mu\text{g/mL}$ anti-h-IgG to adsorbed h-IgG
	SiO <sub>2</sub> -TiO <sub>2</sub>	[55]		15 $\mu\text{g/L}$ terbutryn (pesticide) in a competitive assay
	SiO <sub>2</sub> -TiO <sub>2</sub>	[56]		10–150 $\mu\text{g/mL}$ mouse IgG to immobilized anti-mouse IgG
	Ta <sub>2</sub> O <sub>5</sub>	[57]		0.8–7 $\mu\text{g/mL}$ mouse IgG in competitive assay format $M_r = 2,000$ Da (biotinylated somatostatin)
Output Reflected mode	SiO <sub>2</sub> -TiO <sub>2</sub>	[27]	$3 \times 10^{-6}$	4 $\mu\text{g/mL}$ anti-h-IgG to adsorbed h-IgG
	Ta <sub>2</sub> O <sub>5</sub>	[30]	$3 \times 10^{-6}$	0.2 $\mu\text{g/mL}$ ; $1.4 \times 10^{-9}$ M h-IgG (to adsorbed protein G)
	Ta <sub>2</sub> O <sub>5</sub>	[18]	$3 \times 10^{-6}$	10 $\text{pg/mm}^2$ BSA-biotin/streptavidin-multilayer, 0.25 $\mu\text{g/L}$ simazine (herbicide) inhibition assay
Input and output	Ta <sub>2</sub> O <sub>5</sub>	[19]	$<10^{-6}$	0.3 $\text{pg/mm}^2$ biotin to immobilized neutravidin
Colorimetric resonant reflection	Si <sub>3</sub> N <sub>4</sub> <sup>a</sup>	[31]		$3.4 \times 10^{-5} \Delta n$ (determined by solvents with defined refractive index); 0.4 $\text{pg/mm}^2$ dried BSA; $\sim 0.1$ – $1.0$ $\text{ng/mL}$ streptavidin to immobilized biotin

<sup>a</sup>Also Ta<sub>2</sub>O<sub>5</sub> and TiO<sub>2</sub> in other publications used

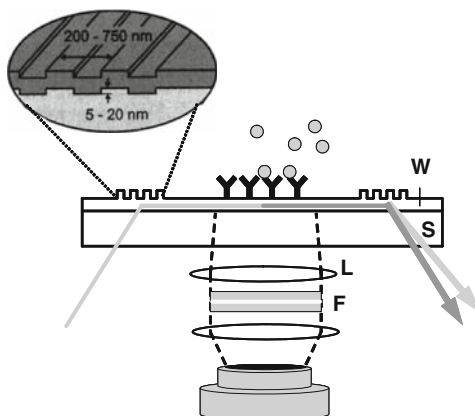
**Table 2** Different detection limits of various interferometric systems

Type	Waveguide material	Citation	Detection limit ( $\Delta n_{\text{eff, min}}$ )	Detection limit by model system
Mach-Zehnder	Si <sub>3</sub> N <sub>4</sub>	[58]	$4 \times 10^{-7}$	$2 \times 10^{-5} \Delta n$ (glucose solution)
Young	SiO <sub>x</sub> N <sub>y</sub>	[11]	$9 \times 10^{-8}$	750 $\text{fg/mL}$ ; 130 $\text{pM}$ (50 $\text{ng/mL}$ IgG to adsorbed protein G)
	Si <sub>3</sub> N <sub>4</sub>	[37]	$2 \times 10^{-8}$	Glucose solution
	Ta <sub>2</sub> O <sub>5</sub>	[20]	$9 \times 10^{-9}$	13 $\text{fg/mm}^2$ ; 390 $\text{fM}$ IgG (to adsorbed protein G)

### 6.3 Evanescent Field Fluorescence

The utilization of fluorescence dyes for analytical measurements enhances the sensitivity for the detection of the molecules of interest. First, Cronick and Little made use of evanescent wave excitation for a fluorescence immunoassay, in 1975. By using totally internally reflected light, they excited the fluorescence of a fluorescein-labeled antibody which has become bound to a hapten–protein conjugate adsorbed on a quartz-plate in an antibody solution [41]. Contrary to the label-free high-refractive-index sensors where the mass of the molecule of interest is

**Fig. 15** Detection principle of evanescent-field fluorescence on planar waveguides: excitation light is coupled into a thin-film waveguide; surface confined fluorescence of bound labeled molecules is detected by a CCD camera. The fluorescence could be also separated via the outcoupling grating and detected by a photodiode. W: waveguide, L: lens, F: filter.



crucial, the sensitivity of the evanescent field fluorescence depends, in addition to the number of capture sites and affinity constants, especially, on the fluorescence dye. The higher the molar extinction coefficient and the number of fluorescent reporter molecules, the more sensitive is the fluorescence detection system. This is common to conventional fluorescence imaging systems. Yet, the illumination for the fluorescence excitation is limited to the thin evanescent field above the waveguide surface.  $\text{Ta}_2\text{O}_5$  or  $\text{SiO}_2\text{-TiO}_2$  are typical high-refractive-index compounds for this purpose [42]. The optical arrangement consists of beam forming optics for light coupling, including the interference filters for the excitation wavelength, and detection optics, including an emission filter to focus the image onto a CCD chip similar to a microscope or a scanning unit with a photodetector (Fig. 15). The evaluation of the fluorescence image is identical to the procedure used in biochip processing. Since the fluorescence excitation is confined to the evanescent field above the waveguide, the assay can be carried out in the presence of the sample. Furthermore, this method is suitable to immobilize the molecule or object of interest, e.g., a biological membrane fragment onto the surface and apply various potential binding partners to the probe. Many different sample solutions independent of pH or solvent can be conveyed sequentially. Independent from biochip or microscopic applications, the signal-to-noise ratio is enhanced by a factor of 100 compared to conventional epifluorescence [42–44]. The reported limit of detection is a spotted concentration of 2 pM Cy5-labeled immunoglobulin G per 150- $\mu\text{m}$ -diameter-spot, corresponding to an amount of 0.8 zeptomole antibody or 500 protein molecules at a dye/protein ratio of  $\sim 5$ . The performance of this system was demonstrated by multiple marker quantification. A set of three cytokines, human interleukins IL-2, IL-4, and IL-6, were simultaneously measured on an antibody array as multiplexed sandwich immunoassay equivalent to an enzyme-linked immunosorbent assay (ELISA). The determined limits of detection are in the range of 1–15 pg/mL for all three investigated interleukins with a variation of signals within one microarray of  $<10\%$ . Regarding the chip-to-chip uncertainty, the assay precision showed a coefficient of variation  $\leq 15\%$  [44].

But also other materials with lower refractive indices enabling total internal reflectance like glass slides can be applied as transducer. Then, an expanded laser beam can be launched into the edge of a microscope slide, thus providing even fluorescence excitation within the evanescent field [45].

## 7 Commercial Sensor Systems

In recent years, biosensors based on waveguide technology have attracted increasing attention due to their versatility and ability for use in medium and high throughput applications. Some of them took the step into commercialization and have to prove of value for industrial applications.

Farfield Sensors Ltd (Crewe, UK) developed the so-called *AnaLight*® sensor system based on dual polarization interferometry applying planar silicon oxynitride waveguides (<http://www.farfield-scientific.com>). A He–Ne laser illuminates the end-face of slab waveguide stack consisting of the sensor waveguide and the reference waveguide buried beneath after passing a ferroelectric liquid crystal half plate that switches the state of polarization between TE and TM. Since the distance between the two waveguides is only a few hundred micrometers, the diffracting light beams at the end of the stack generate the Young interference pattern that is recorded by a high-resolution CCD camera. The image data are synchronized with the polarization state and processed by a spatial Fourier transformation analysis. The system measures the thickness of an adsorbing layer with a resolution of  $<0.01$  nm corresponding to  $0.1$  pg/mm<sup>2</sup> [46]. The fluidic handling is based on a pump that conveys the sample to the sensing waveguide. An adaptation to the widespread standard microtiter plate format, such as the 96-well and the 384-well microplates, is not available and seems challenging since the single wells cannot be separately accessed. But a parallelization is imaginable since the physical principle itself does not require moving parts so that the optical readout could scan several sensor areas.

The Centre Suisse d'Electronique et de Microtechnique SA (CSEM) developed the WIOS (wavelength-interrogated optical sensor) system based on the grating coupling method for the real-time observation of biomolecular interactions (<http://www.csem.ch>). It is a small bench-top system with normally 4–8 parallel fluidic channels for the label-free determination of binding interactions. High-refractive-index waveguide gratings with different grating periods of 300–700 nm for the coupling areas (input and output pad) are used as optical transducer. The mass coverage can be detected to a lower detection limit of 300 fg/mm<sup>2</sup>.

SRU Biosystems (Woburn, MA) applied the principle of the colorimetric resonant grating reflection in the so-called BIND<sup>TM</sup> (Biomolecular Interaction Detection) system that allows parallel readout in 96- and 384-well microplate format (<http://www.srubiosystems.com>). A grating with a period shorter than the reflected wavelength range (550 nm) and a depth in the range of 170 nm is structured by

a silicon master wafer on liquid epoxy resin. The silicon wafer was etched in a shape that can be used as a replication mold for the liquid resin that is squeezed between the wafer and a polymer foil. After curing by UV light, the solid grating structure is peeled away from the silicon master.  $\text{TiO}_2$ , a high-refractive-index dielectric material, is sputtered on the surface structure to obtain the final sensor surface. Both the molding replication and the sputter process can be carried out on a continuous plastic sheet of several hundred meters in length. The  $\text{TiO}_2$  surface with an optical grating creates a very sharp optical reflection at a particular wavelength that can be accurately traced as biological molecules bind to the surface. The signal is measured as the shift of the peak wavelength value ( $\Delta\text{PWV}$ ). Using low-cost components, the sensor is able to resolve protein mass changes on the surface with a resolution less than  $1 \text{ pg/mm}^2$  [47].

Corning Incorporated (<http://www.corning.com>) introduced with the Epic<sup>®</sup> system, a resonant waveguide grating (RWG) biosensor system, as a label-free high throughput screening platform for biochemical and cell-based drug discovery [22]. It is very similar to the colorimetric resonant grating reflection system by SRU Biosystems but applies  $\text{Nb}_2\text{O}_5$  as waveguide material. The thin grating structure of  $\sim 75\text{--}100 \text{ nm}$  thickness is deposited on a glass substrate that is integrated as the bottom in a 96- or 384-well microplate. The assay sensitivity is stated as  $5 \text{ pg/mm}^2$ . Cells that adhere to the sensor surface by the extracellular matrix were studied upon various stimulations. The change of the refractive index within the part of the cell that is entered by the evanescent wave is monitored and evaluated depending on the experimental approach [21].

Zeptosens (a division of Bayer AG, <http://www.zeptosens.com/en/>) developed the ZeptoREADER for microarray applications based on glass slides with a  $\text{Ta}_2\text{O}_5$  waveguide for evanescent fluorescence excitation [48]. The system is designed to be applied for spatially resolved fluorescence emission analysis. The setup exhibits a surface-confined, very strong electromagnetic field for efficient and selective excitation of fluorescent labels on the surface. An incident laser beam (635, 532, and 492 nm optional) is coupled into a  $\text{Ta}_2\text{O}_5$  waveguide on top of a transparent substrate, via a diffractive grating. The evanescent field with a penetration depth of about 200 nm into the adjacent medium ensures that only fluorophores close to the surface are excited, which leads to an improvement of the signal-to-noise ratio as well as a highly sensitive and precise measurement. The fluorescence emission light is collected by an objective and focused on a CCD camera enabling imaging of waveguide chip areas of about  $5 \text{ mm} \times 7 \text{ mm}$ , leading to microarray applications. A filter wheel with interference filters selects the emission wavelength of the applied fluorophores. For medium and high throughput applications, Zeptosens equipped the system with a stacker capable of holding waveguide chips or carriers adapted to the 96-well plate format arranging five chips. Furthermore, they can use a 96-well plate consisting of a base plate with the waveguide structure and a mounted plastic 96-well structure. The sample can be applied using manual or robotic multipipettors or by a flow-cell.

## 8 Applications

Optical biosensors based on high-refractive-index waveguides can be applied in biotechnological and pharmaceutical research for target analysis, drug discovery, drug development, and disease diagnostics. Therefore, highly parallel and sensitive measurement systems are needed for a reliable investigation of DNA and proteins. Due to their consumption of small sample volumes, sensor systems using array formats can achieve a low price per test with high specificity and sensitivity. Depending on the application, they can be not only integrated in automatic high throughput analysis but also used for highly sensitive experiments in the research laboratory. The systems exhibit accessibility for the add-on of flow cells or pipetting devices. High-refractive-index sensor platforms in various extensions were developed with the advantage of high sensitivity and measurement in presence of the sample without any rinsing. The spatially limited evanescent field at the surface can be applied for both surface-confined fluorescence excitation and label-free detection of refractive index changes [49].

Microarray technologies based on imaging detecting optics enable the parallel measurement of a huge number of different biomolecules. In pharmaceutical and medical research, microarrays are applied for gene screening to detect novel drug targets, for gene expression monitoring to identify disease-specific genes, and for the determination of toxic effects of drug candidates. Furthermore, gene mutations and single nucleotide polymorphisms can be detected. In case of DNA microarrays, the interaction is limited to polynucleotide sequences or chemically similar polymers. Proteins are considerably more complex but they offer more insight into the real nature of disease and drug action. While DNA can be amplified by polymerase chain reaction, a similar tool does not exist for proteins so that low detection limits are required. Protein microarrays address various interactions of ligand–receptor pairs, such as antibody–antigen, enzyme–substrate, cell membrane receptor–ligand, protein–protein/peptide or protein–DNA/RNA [48].

Similar to mRNA, most of the cell proteins (up to 90%) are believed to be present as low copy numbers [50]. Therefore, when no amplification is possible, the highly sensitive evanescent field fluorescence technology is a promising solution to reliably measure low abundance proteins enabling detection of molecules at the picomolar level [44]. Capture molecules are immobilized for sandwich-like assays consisting of a capture antibody, the molecule (e.g., protein, antibody) of interest, and a secondary reporter antibody. A multiplexed immunoassay of this kind was developed for simultaneous quantitative monitoring of cancer biomarkers in tissue extracts on the Zeptosens platform [51]. Another approach is the spotting of the cell lysate on a hydrophobized waveguide and the subsequent incubation with a specific antibody and a secondary reporter antibody, e.g., for the investigation of tumor markers by spots of lysates of tumor and normal tissue and incubation with tumor-specific antibodies [52]. If an evanescent field fluorescence system is furnished with a suitable microscope objective, the distribution of any dye labeling a reporter antibody or similar molecules in a sample, e.g., cell membrane, can be investigated.

The feasibility was demonstrated on human fibroblast cells fixed and stained for vinculin, a focal adhesion protein [42].

In pharmaceutical research, the determination of affinity constants is a crucial step in the development of antibodies and also for affinity studies of new target molecules. Surface plasmon resonance systems are a widespread technology applied for this purpose [53, 54]. Waveguide sensors provide also an excellent tool for highly sensitive label-free detection of biomolecules. Various types of grating coupler systems and interferometric systems are suitable for the investigation of binding events in a label-free manner. On the basis of an antibody–antigen interaction, the determination of binding constants was shown [35]. Furthermore, chemical environmental pollutants such as herbicides or fungicides, as small molecules, can be detected at very low concentrations.

Generally, the application of a sensor system is determined by the chemical or biological recognition elements. They have to fulfill the following requirements:

*Sensitivity:* The limit of detection for a certain compound is determined by its affinity constant or binding constant to the interaction partner immobilized to the surface. Therefore, the choice of the capture compound affects remarkably the assay performance. Because of the opportunity to create antibodies against different kind of compounds, e.g., peptides, proteins, enzymes, vitamins, environmental pollutants, herbicides, fungicides, etc., they are frequently used as a versatile tool for sensor assay developments.

*Specificity:* An important criterion is also how specifically the capture molecule binds its interaction partner molecule. Nonspecific binding of matrix molecules to the sensing layer leads to false positive signals causing an error in the measurement values. Control experiments with compounds that show nonspecific adsorption, e.g., bovine serum albumin (BSA), are recommended. Blocking of the surface, meaning that a layer of e.g., BSA prevents the nonspecific adsorption of other matrix molecules and is displaced by the molecule interacting specifically, can also enhance the specificity in an assay.

*Stability:* Often, a regeneration of the sensor surface is desirable so that several samples can be measured with the same sensor surface. Therefore, regeneration solutions for stringent washing of the surface are applied, e.g., solutions with low pH or a considerable amount of detergents. The comparability between the assays performed with the identical sensor surface requires a sufficient stability against these chemical conditions.

A further issue is the steric hindrance: the interaction properties in a homogeneous assay are not directly transferable to the binding conditions at a surface/interface. The binding site of an immobilized capture molecule is accessible only from one side. It must be exposed on the surface in an optimal manner. Likewise, the capturing partner, e.g., peptide or protein, should be oriented with its binding-active domain toward the sample solution.

High-refractive-index platforms have a very broad application range, comprising microarray technologies, assays in microwell plate format, and binding studies in a flow cell if the aforementioned issues are taken into account.

## 9 Concluding Remarks

Optical chemical and biosensors have proven to be very sensitive, stable, and reliable detection systems, in the recent years. The sensor platforms based on high-refractive-index waveguides can be applied successfully for both label-free and fluorescence-based detection. Label-free techniques abate the uncertainty induced by the effect of the label on molecular conformation, inaccessibility of active binding sites due to the label, steric hindrance, or the inability to find an appropriate label that functions equivalently for all molecules in the experiment. Yet, the drawback of nonspecific binding retards the implementation of the label-free techniques as standard instrumentation for high throughput screening. Pharmaceutical screening involves the detection of small molecules as drug candidates where the limit of detection is important and the detection of proteins where the prevention of nonspecific binding is crucial. Even though some suppliers, e.g., SRU Biosystems or Corning Inc., offer technical solutions for this purpose, label-free sensors are not yet routinely applied for binding studies in a highly parallel format. The high costs for the fabrication of the optical transducers play a key role for the implementation in screening applications. However, label-free sensors are perfectly suited for the determination of affinity constants since the binding reaction is not disturbed by any label. The utilization of the evanescent field fluorescence techniques improved the limit of detection for microarray applications considerably and simplified the sample preparation because of the confined illumination of the dye-labeled molecules at the sensor surface. Targeted development for specific applications, e.g., point-of-care devices or diagnostics, will lead to a broader distribution of high-refractive-index sensor platforms.

## References

1. Baird CL, Myszkowski DG (2001) Current and emerging commercial optical biosensors. *J Mol Recogn* 14:261–268
2. Keusgen M (2002) Biosensors: new approaches in drug discovery. *Naturwissenschaften* 89:433–444
3. Nice EC, Catimel B (1999) Instrumental biosensors: new perspectives for the analysis of biomolecular interactions. *BioEssays* 21:339–352
4. Saleh BEA, Teich MC (2007) Fundamentals of photonics. Wiley, New York
5. Snyder AW, Love JD (1983) Optical waveguide theory. Chapman and Hall, London
6. Kogelnik H (1988) Theory of optical waveguides. Springer, New York, Berlin, Heidelberg
7. Tiefenthaler K, Lukosz W (1989) Sensitivity of grating couplers as integrated-optical chemical sensors. *J Opt Soc Am B* 6:209–220
8. Schmitt K (2006) A new waveguide interferometer for the label-free detection of biomolecules. PhD thesis, Université Louis Pasteur, Strasbourg
9. Hu H, Lu F, Chen F, Shi B-R, Wang K-M, Shen D-Y (2001) Monomode optical waveguide in lithium niobate formed by MeV Si<sup>+</sup> ion implantation. *J Appl Phys* 89:5224–5226

10. Korishko YN, Fedorov VA, Feoktistova OY (2000) LiNbO<sub>3</sub> Optical waveguide fabrication by high-temperature proton exchange. *J Lightwave Technol* 18:562–568
11. Brandenburg A, Krauter R, Künzel C, Stefan M, Schulte H (2000) Interferometric sensor for detection of surface-bound bioreactions. *Appl Opt* 39:6396–6405
12. Germann R, Salemink HWM, Beyeler R, Bona GL, Horst F, Massarek I, Offrein BJ (2000) Silicon oxynitride layers for optical waveguide applications. *J Electrochem Soc* 147:2237–2241
13. Gorecki C (2000) Optimization of plasma-deposited silicon oxynitride films for optical channel waveguides. *Opt Lasers Eng* 33:15–20
14. Wörhoff K, Lambeck PV, Driessen A (1999) Design, tolerance analysis, and fabrication of silicon oxynitride based planar optical waveguides for communication devices. *J Lightwave Technol* 17:1401–1407
15. Lukosz W (1991) Principles and sensitivities of integrated optical and surface plasmon sensors for direct affinity sensing and immunosensing. *Biosens Bioelectron* 6:215–225
16. Höök F, Vörös J, Rodahl M, Kurrat R, Böni P, Ramsden JJ, Textor M, Spencer ND, Tengvall P, Gold J, Kasemo B (2002) A comparative study of protein adsorption on titanium oxide surfaces using in situ ellipsometry, optical waveguide lightmode spectroscopy, and quartz crystal microbalance/dissipation. *Colloids Surf B Biointerfaces* 24:155–170
17. Heideman RG, Lambeck PV (1999) Remote opto-chemical sensing with extreme sensitivity: design, fabrication and performance of a pigtailed integrated optical phase-modulated Mach-Zehnder interferometer system. *Sensors Actuators B Chem* 61:100–127
18. Piehler J, Brandenburg A, Brecht A, Wagner E, Gauglitz G (1997) Characterization of grating couplers for affinity-based pesticide sensing. *Appl Opt* 36:6554–6562
19. Cottier K, Wiki M, Voirin G, Gao H, Kunz RE (2003) Label-free highly sensitive detection of (small) molecules by wavelength interrogation of integrated optical chips. *Sensors Actuators B Chem* 91:241–251
20. Schmitt K, Schirmer B, Hoffmann C, Brandenburg A, Meyrueis P (2007) Interferometric biosensor based on planar optical waveguide sensor chips for label-free detection of surface bound bioreactions. *Biosens Bioelectron* 22:2591–2597
21. Fang Y (2007) Non-invasive optical biosensor for probing cell signaling. *Sensors* 7:2316–2329
22. Fang Y, Ferrie AM, Fontaine NH, Yuen PK (2005) Characteristics of dynamic mass redistribution of epidermal growth factor receptor signaling in living cells measured with label-free optical biosensors. *Anal Chem* 77:5720–5725
23. Tamir T, Peng ST (1977) Analysis and design of grating couplers. *Appl Phys* 14:235–254
24. Lukosz W, Tiefenthaler K (1984) Directional switching in planar waveguides effected by adsorption-desorption processes. In: *Proceedings of 2nd european conference on integrated optics*, Florence, Italy
25. Nellen PM, Lukosz W (1990) Integrated optical input grating couplers as chemo- and immunosensors. *Sensors Actuators B Chem* 1:592–596
26. Nellen PM, Tiefenthaler K, Lukosz W (1988) Integrated optical input grating couplers as biochemical sensors. *Sensors Actuators* 15:285–295
27. Lukosz W, Clerc D, Nellen PM, Stamm C, Weiss P (1991) Output grating couplers on planar optical waveguides as direct immunosensors. *Biosens Bioelectron* 6:227–232
28. Lukosz W, Nellen PM, Stamm C, Weiss P (1990) Output grating couplers on planar waveguides as integrated optical chemical sensors. *Sensors Actuators B Chem* 1:585–588
29. Brandenburg A, Gombert A (1993) Grating couplers as chemical sensors: a new optical configuration. *Sensors Actuators B Chem* 17:35–40
30. Brandenburg A, Polzius R, Bier F, Bilitewski U, Wagner E (1996) Direct observation of affinity reactions by reflected-mode operation of integrated optical coupler. *Sensors Actuators B Chem* 30:55–59
31. Cunningham B, Li P, Lin B, Pepper J (2002) Colorimetric resonant reflection as a direct biochemical assay technique. *Sensors Actuators B Chem* 81:316–328
32. Cunningham B, Qiu J, Li P, Lin B (2002) Enhancing the surface sensitivity of colorimetric resonant optical biosensors. *Sensors Actuators B Chem* 6779:1–6



33. Li PY, Lin B, Gerstenmaier J, Cunningham BT (2004) A new method for label-free imaging of biomolecular interactions. *Sensors Actuators B Chem* 99:6–13
34. Weissner M, Tovar G, Mittler-Neher S, Knoll W, Brosinger F, Freimuth H, Lacher M, Ehrfeld W (1999) Specific bio-recognition reactions observed with an integrated Mach-Zehnder interferometer. *Biosens Bioelectron* 14:405–411
35. Hoffmann C, Schmitt K, Brandenburg A, Hartmann S (2007) Rapid protein expression analysis with an interferometric biosensor for monitoring protein production. *Anal Bioanal Chem* 387:1921–1932
36. Schneider BH, Edwards J, Hartman N (1997) Hartman interferometer: versatile integrated optic sensor for label-free, real-time quantification of nucleic acids, proteins, and pathogens. *Clin Chem* 43:1757–1763
37. Ymeti A, Kanger JS, Wijn R, Lambeck PV, Greve J (2002) Development of a multichannel integrated interferometer immunosensor. *Sensors Actuators B Chem* 83:1–7
38. Cross GH, Reeves AA, Brand S, Popplewell JF, Peel LL, Swann MJ, Freeman NJ (2003) A new quantitative optical biosensor for protein characterisation. *Biosens Bioelectron* 19:383–390
39. Cross GH, Ren Y, Freeman NJ (1999) Young's fringes from vertically integrated slab waveguides: applications to humidity sensing. *J Appl Phys* 86:6483–6488
40. Stamm C, Dangel R, Lukosz W (1998) Biosensing with the integrated-optical difference interferometer: dual-wavelength operation. *Opt Commun* 153:347–359
41. Kronick MN, Little WA (1975) A new immunoassay based on fluorescence excitation by internal reflection spectroscopy. *J Immunol Methods* 8:235–240
42. Grandin HM, Staedler B, Textor M, Vörös J (2006) Waveguide excitation fluorescence microscopy: A new tool for sensing and imaging the biointerface. *Biosens Bioelectron* 21:1476–1482
43. Neuschäfer D, Budach W, Wanke C, Chibout S-D (2003) Evanescent resonator chips: a universal platform with superior sensitivity for fluorescence-based microarrays. *Biosens Bioelectron* 18:489–497
44. Pawlak M, Schick E, Bopp MA, Schneider MJ, Oroszlan P, Ehrat M (2002) Zeptosens' protein microarrays: A novel high performance microarray platform for low abundance protein analysis. *Proteomics* 2:383–393
45. Ligler FS, Sapsford KE, Golden JP, Shriver-Lake LC, Taitt CR, Dyer MA, Barone S, Myatt CJ (2007) The array biosensor: portable, automated systems. *Anal Sci* 23:5–10
46. Ronan G (2004) Doubling up: dual polarization interferometry determines protein structure and function. *SPIE's oemagazine* 17–20
47. Cunningham BT, Li P, Schulz S, Lin B, Baird C, Gerstenmaier J, Genick C, Wang F, Fine E, Laing L (2004) Label-free assays on the BIND system. *J Biomol Screen* 9:481–490
48. Ehrat M, Kresbach GM (2001) DNA and protein microarrays and their contributions to proteomics and genomics. *Chimia* 55:35–39
49. Schmitt K, Oehse K, Sulz G, Hoffmann C (2008) Evanescent field sensors based on tantalum pentoxide waveguides – a review. *Sensors* 8:711–738
50. Miklos GL, Maleszka R (2001) Protein functions and biological contexts. *Proteomics* 1: 169–178
51. Weissenstein U, Schneider MJ, Pawlak M, Cienas J, Eppenberger-Castori S, Oroszlan P, Ehret S, Geurts-Moespot A, Sweep FCGJ, Eppenberger U (2006) Protein chip based miniaturized assay for simultaneous quantitative monitoring of cancer biomarkers in tissue extracts. *Proteomics* 6:1427–1436
52. Templin MF, Stoll D, Pawlak M, Joos TO (2006) Protein microarrays: Neue Systeme für die Proteomforschung. *GIT Labor-Fachzeitschrift* 50:890–892
53. Homola J, Vaisocherová H, Dostálek J, Piliarik M (2005) Multi-analyte surface plasmon resonance biosensing. *Methods* 37:26–36
54. Rich RL, Myszkowski DG (2005) Survey of the year 2003 commercial optical biosensor literature. *J Mol Recogn* 18:1–39

55. Bier FF, Jockers R, Schmid RD (1994) Integrated optical immunosensor for s-triazine determination: regeneration, calibration and limitations. *Analyst* 119:437–441
56. Polzius R, Bier FF, Bilitewski U, Jäger V, Schmid RD (1993) On-line monitoring of monoclonal antibodies in animal cell culture using a grating coupler. *Biotech Bioeng* 42:1287–1292
57. Polzius R, Dießel E, Bier F, Bilitewski U (1997) Real-time observation of affinity reactions using grating couplers: determination of the detection limit and calculation of rate constants. *Anal Biochem* 248:269–276
58. Prieto F, Sepúlveda B, Calle A, Llobera A, Domínguez C, Lechuga LM (2003) Integrated Mach-Zehnder interferometer based on ARROW structures for biosensor applications. *Sensors Actuators B Chem* 92:151–158



<http://www.springer.com/978-3-540-88241-1>

Optical Guided-wave Chemical and Biosensors I

Zourob, M.; Lakhtakia, A. (Eds.)

2009, XVI, 234 p., Hardcover

ISBN: 978-3-540-88241-1